1 RESEARCH ARTICLE

2 Evaluation of thrust measurement techniques for dielectric
3 barrier discharge actuators

4 **Ryan Durscher · Subrata Roy**

7 **Abstract** Despite its popularity in the recent literature,
8 plasma actuators lack a consistent study to identify limi-
9 tations, and remedy thereof, of various thrust measurement
10 techniques. This paper focuses on comparing two different
11 experimental techniques commonly used to measure the
12 global, plasma-induced thrust. A force balance is used to
13 make a direct measurement of the thrust produced, which is
14 then compared with a control volume analysis on data
15 obtained through particle image velocimetry. The local
16 velocity measured by particle image velocimetry is also
17 validated with a fine-tip pressure probe. For the direct
18 thrust measurements, the effect of varying the actuator
19 plate length upon which the induced flow acts is investi-
20 gated. The results from these tests show that the length of
21 the actuator plate is most influential at higher voltages with
22 the measured thrust increasing as much as 20 % for a six
23 times reduction in the length of the plate. For the indirect
24 thrust measurement, the influence of the control volume
25 size is analyzed. When the two methods are compared
26 against each other, good agreement is found when the
27 control volume size has a sufficient downstream extent.
28 Also, the discharge length is optically measured using
29 visible light emission. A linear correlation is found
30 between the discharge length and the thrust measurements
31 for the actuator configurations studied. Finally, the energy
32 conversion efficiency curve for a representative actuator is
33 also presented.
34

A1 R. Durscher · S. Roy (✉)
A2 Applied Physics Research Group, Mechanical and Aerospace
A3 Engineering Department, University of Florida, Gainesville,
A4 FL 32611-6300, USA
A5 e-mail: roy@ufl.edu

1 Introduction

35

The dielectric barrier discharge (DBD) plasma actuator, in 36
general, consists of an asymmetric electrode arrangement 37
(one exposed and one encapsulated) separated by a 38
dielectric medium. The application of an alternating, high- 39
voltage signal results in a surface-mode discharge along the 40
dielectric. At (or near) atmospheric pressures, the discharge 41
is comprised of micro-discharges which form discrete 42
channels between the electrode and dielectric surface 43
(Gibalov and Pietsch 2000; Kogelschatz 2003; Xu 2001). 44
The expansion of the discharge along the dielectric surface 45
results in a charge deposition, which in turn reduces the 46
local electric field and extinguishes the micro-discharge. 47
Collectively, the discharge is completely extinguished 48
twice per period as evident by the light emission and dis- 49
charge current (Enloe et al. 2004). As the ionized particles 50
within the micro-discharges propagate along the dielectric 51
surface, momentum is transferred to the surrounding neu- 52
tral particles through a poorly understood collisional 53
mechanism. Macroscopically, however, the net separated 54
space charge within the plasma interacts with the electric 55
field resulting in an electro-hydrodynamic body force act- 56
ing on the working gas resulting in an acceleration of the 57
fluid. By virtue of Newton's third law, an equal and 58
opposite force is imparted to the actuator. Experiments 59
have shown this momentum exchange to be cyclic with the 60
magnitude of the force varying depending on the polarity 61
of the exposed electrode (Debien et al. 2012, Enloe et al. 62
2008b; Enloe et al. 2009; Font et al. 2011). 63

The plasma actuator has been used as a flow control 64
mechanism in various aerodynamic applications such as 65
turbines blades (Ramakumar and Jacob 2005; Rizzetta and 66
Visbal 2008), landing gears (Thomas et al. 2005), airfoils 67
(Little et al. 2010; Post and Corke 2004), turbulent jets 68

(Labergue et al. 2007), and an assortment of conical flows (e.g. flat plate boundary layers (Gibson et al. 2012; Grundmann and Tropea 2009; Roth et al. 2000; Schatzman and Thomas 2010), cylinder vortex shedding (Jukes and Choi 2009; Thomas et al. 2008), etc.). In order to improve the fluidic authority of the actuators, numerous parametric studies have been undertaken which have focused on various aspects (e.g. applied voltage/frequency, dielectric material, electrode arrangement) of the actuator (Abe et al. 2008; Borghi et al. 2008; Corke et al. 2007; Forte et al. 2007; Hoskinson and Hershkowitz 2010; Hoskinson et al. 2008; Jolibois and Moreau 2009; Roth and Dai 2006; Thomas et al. 2009). Characterizing the resulting induced thrust is therefore pivotal for understanding the influence of various control parameters in improving the actuator authority.

Several methods have been employed for measuring the plasma-induced thrust. Typically, a simplified approach is used to either measure the net thrust directly using a high resolution ($\sim$ mg) force balance or calculate it indirectly based on the velocity field extracted using techniques such as Pitot probes, particle image velocimetry (PIV), and laser Doppler velocimetry (LDV). Specifically, the latter approach relies on a control volume analysis of the measured flow field to determine the net thrust produced (Baughn et al. 2006; Hoskinson et al. 2008; Kotsonis et al. 2011; Kriegseis 2011a; Debien et al. 2012). Recently, more complicated methods have also been investigated that resolves the plasma body force spatially by applying the Navier–Stokes momentum equations to PIV data (Kotsonis et al. 2011). However, a basic study aimed at the limitations of the simplified direct or indirect measurements is lacking. For example, the near wall flow as a result of actuation gives rise to a self-induced drag (Font et al. 2010), for which the plate size would likely have a significant impact on the measured thrust. The plate size, however, is not typically reported in the literature. Also, how does the calculated thrust vary with the size of control volume, and how does it compare with the direct measurement? In literature, a comparison between the two methods is often met with mixed results. Hoskinson et al. (2008) reported a factor of two difference in the calculated thrust between the two techniques (attributed to simplifications made), while Kotsonis et al. (2011) showed a reasonable agreement between the two methods.

This paper focuses on characterizing some limitations of the aforementioned direct and control volume inferred experimental techniques used to measure the net, induced thrust for a basic single dielectric barrier discharge (SDBD) actuator configuration. In particular, the influence of the plate size on the direct thrust measurement is investigated. Similarly, the thrust is indirectly determined from a control volume analysis of the flow field obtained through PIV.

Here, the influence of the control volume size on the calculated thrust is analyzed by comparing with the plate size–independent direct thrust data. Also, the discharge length is optically measured using visible light emission. A functional relationship between the measured discharge length and the measured thrust is studied. The local velocity measured by the PIV technique is also validated with Pitot tube measurements at different locations. The paper is organized in the following manner. Section 2 describes the experimental setup for the tests conducted. This includes a discussion of the direct thrust measuring arrangement, PIV details, and the control volume analysis. Section 3 presents the results for the aforementioned investigations, while conclusions are drawn in Sect. 4.

2 Experimental arrangement

2.1 Plasma actuator design and discharge generation

A cross-sectional schematic of the DBD plasma actuator used in these experiments is shown in Fig. 1a. The actuator

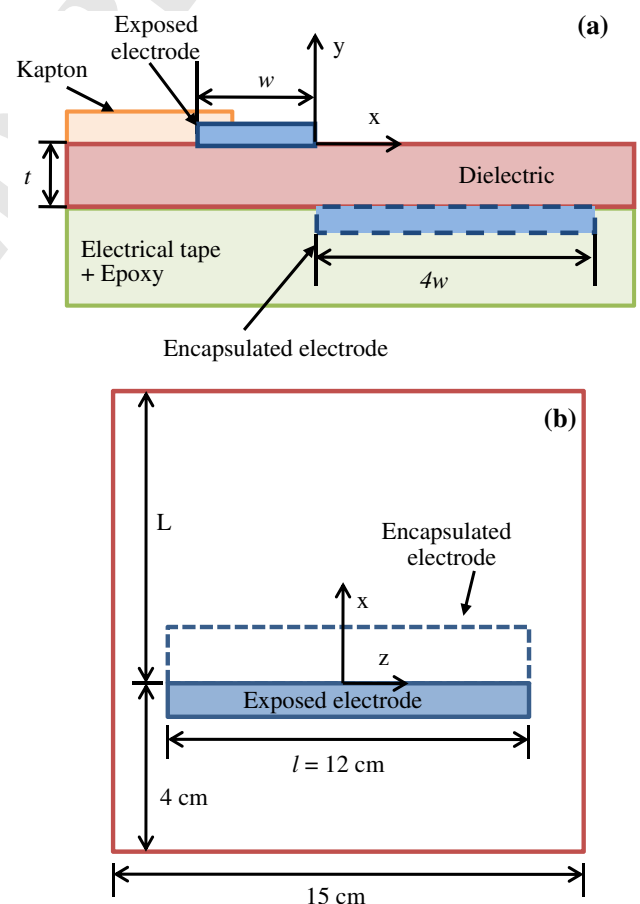**Fig. 1** Schematic of DBD plasma actuator: **a** *side view* and **b** *top view* (not drawn to scale)
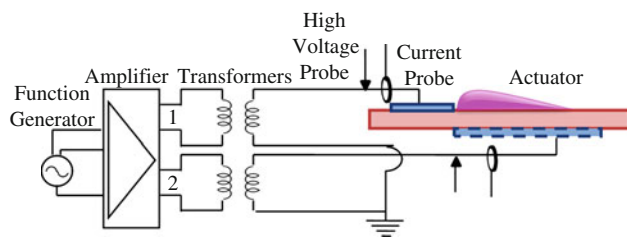
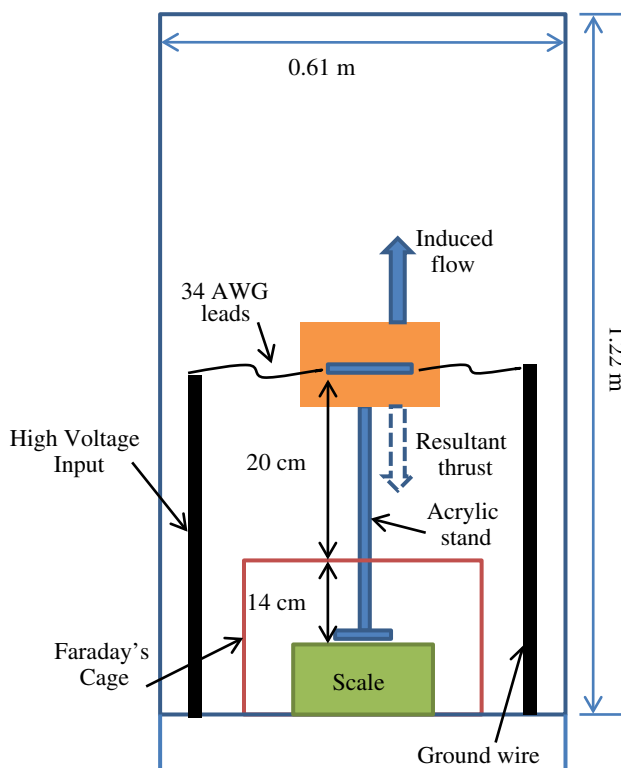**Fig. 2** Circuit schematic used to generate a DBD plasma discharge

Fig. 3 Experimental setup schematic for direct force measurement

140 consists of two thin (70 μm) copper electrodes placed
141 asymmetrically on either side of the dielectric material
142 with no horizontal gap between the two electrodes. The
143 dielectric in this case was a 3-mm-thick (*t*) sheet of acrylic
144 which has a nominal relative dielectric constant of 3. The
145 width, *w*, of the upper electrode was 0.5 cm while the
146 lower electrode's width is 2 cm. Both electrodes have a
147 length, *l*, of 12 cm. Three layers of vinyl electrical tape
148 (178-μm thick) covered the encapsulated electrode to avert
149 an unwanted discharge on the lower surface. Similarly, an
150 84-μm-thick piece of Kapton was placed on the opposite
151 side of the exposed electrode preventing the occurrence of
152 a discharge. The actuator depicted in Fig. 1b shows the
153 dimensions of the dielectric used in the actuator plate
154 length tests, where the effect on the thrust was investigated
155 by shortening the actuator's plate length, *L*.

156 In order to ionize the surrounding air, the exposed and
157 grounded electrodes were each supplied with high-voltage
158 signals that were 180° out of phase. A congruent powering
159 scheme has previously been used by Thomas et al. (2009).
160 The sinusoidal input signals were generated using an
161 arbitrary waveform generator (Tektronix AFG3022B).
162 These signals were further amplified by a dual output audio
163 amplifier (QSC RMX 2450) which was then stepped up
164 using high-voltage transformers (Corona Magnetics, Inc.
165 CMI 5523) (Fig. 2). Actuators were tested with total
166 voltages ranging from 14 to 28 kVpp at two distinct fre-
167 quencies 7 and 14 kHz.

168 The voltage and current supplied to the actuators were
169 monitored using high-voltage (Tektronix P6015A) and
170 current probes (Pearson Electronic 2100). In order to cal-
171 culate the delivered power, the voltage and current wave-
172 forms were captured using a digitizing oscilloscope
173 (Tektronix DPO3014). In a single acquisition, the oscillo-
174 scopes captured 1 million points for each waveform at a
175 sampling rate of 250 MSa s^{-1}. For each input voltage, 10
176 acquisitions were recorded. This corresponds to 280 and
177 560 periods over which the calculated power is averaged
178 for 7 and 14 kHz waveforms, respectively. The total
179 power, *P*, delivered to the plasma actuator was considered
180 to be a linear superposition of the power supplied to each
181 electrode. The average real power was numerically calcu-
182 lated by multiplying the instantaneous voltage, V_i, by the
183 instantaneous current, I_i, and then summing and dividing
184 by the total number of samples, *N*. The indices 1 and 2 in
185 Eq. 1 correspond to the respective circuit branches in
186 Fig. 2.

$$P = \frac{1}{N}\left(\sum_{i=1}^{N} V_{1,i}I_{1,i} + \sum_{i=1}^{N} V_{2,i}I_{2,i}\right) \tag{1}$$

2.2 Direct thrust measurements 188 189

190 Direct thrust measurements were obtained using an Ohaus
191 precision balance (Adventurer^{TM} Pro AV313C). The
192 actuators were mounted to the scale by an acrylic stand
193 which protruded though a small opening in a Faraday's
194 cage (Fig. 3). The cage was constructed using aluminum
195 (3.18-mm thick) and was used to shield the balance from
196 any electromagnetic interference due to the high electric
197 fields required to generate the plasma discharge. To pre-
198 vent ambient room currents from influencing the sensitive
199 scale (of resolution 1 mg), the entire setup was housed in
200 a large quiescent chamber with dimensions 0.61 ×
201 0.61 × 1.22 m (width × depth × height). Thin insulated
202 wire (34 AWG) was used to connect the high-voltage
203 input leads to the actuator in order to limit the rigidity of
204 the wire from influencing the reading. For each input
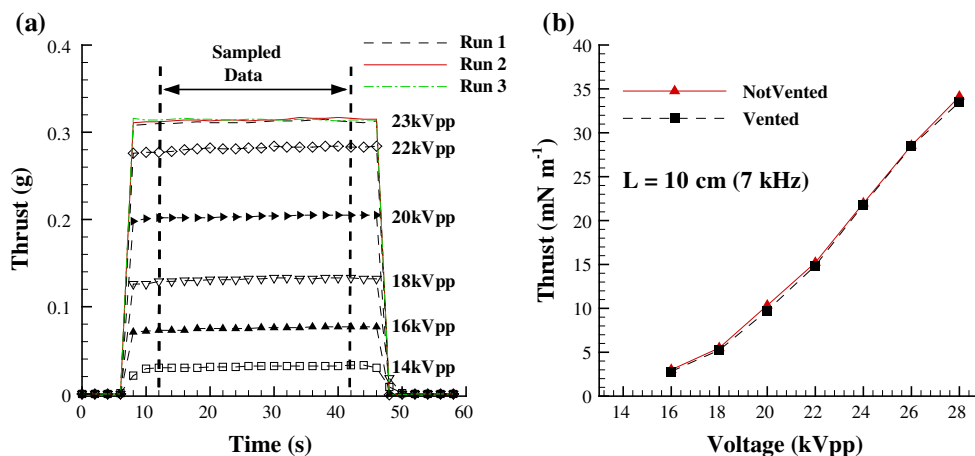205 voltage, 15 measurements were recorded from the scale

Fig. 4 a Example readouts from the balance showing the stability and repeatability of the direct thrust measurement (14 kHz). **b** Effect of a vented versus unvented chamber on the induced thrust (7 kHz). The plate length (*L*) was 10 cm for both plots

206 over a 30-s span once an initial stable reading was
207 reached. An example output from the balance is shown in
208 Fig. 4a for various voltages. The maximum uncertainty
209 associated with a given measurement is estimated to be
210 within 4 % (to 95 % confidence), based on repeated
211 measurements (at a constant voltage) and the scale's
212 inherent uncertainty. Furthermore, the error in the thrust
213 measurement due to the scale's cross-axis sensitivity was
214 investigated and found to be negligible. This was deter-
215 mined by orienting the actuator on the mass balance to
216 measure the z-component of the force (referring to
217 Fig. 1). In such an arrangement, the scale would be
218 affected by both x and y components in the cross-axis
219 direction. Given that the *z*-component should be zero for a
220 linear actuator, a registered thrust reading by the balance
221 should presumably be a result of its sensitivity to cross-
222 axis forces. No thrust was measured as the balance read
223 zero over the entire range of input voltages.
224 Furthermore, the chamber in which the scale is housed is
225 only slightly vented to prevent potentially dangerous
226 amounts of ozone from continuously spreading into the
227 laboratory. As a consequence, one could argue that for
228 particularly long runs of the actuator that the air chemistry
229 inside of the chamber is being modified. To test this
230 argument, two tests were carried out over a range on input
231 voltages. In one case, the 0.74 m² door to the chamber was
232 closed during testing, while it was left wide open in the
233 other. The measured thrust from these tests is shown in
234 Fig. 4b, where "not vented" and "vented" correspond to
235 the door being closed and open, respectively. As evident
236 from the figure, the resultant thrust was nearly identical
237 regardless of ventilation. This result would likely change if
238 the volume of the quiescent of chamber was reduced,
239 though the results seem indifferent for the current experi-
240 mental setup.

3 Control volume analysis 241

3.1 Flow field measurements 242

Two-component PIV was used to generate time-averaged, 243
spatially resolved data of the induced flow due to the 244
plasma actuation. These averaged vector fields were then 245
used for the control volume analysis. The plasma actuator 246
geometry is similar to that described previously (Fig. 1); 247
however, the dielectric plate upon which the actuator was 248
built was much larger. The dimensions of the plate are 249
30 cm × 30 cm with the electrodes placed in the center. 250
The actuator was set up in the same quiescent chamber as 251
described above. 252
A Nd:YAG, dual cavity pulsed 532-nm laser (New 253
Wave Research Solo PIV II 30) was used to generate a 254
light sheet along the centerline of the actuator normal to 255
the span. This illuminated the vaporized Ondina oil used 256
to seed the chamber (see Sect. 7). Adjustable focal length 257
optics allowed for fine adjustments to the waist of the 258
laser sheet, which had an estimated thickness of 1 mm. 259
The time separation (*dt*) between laser pulses was 260
adjusted accordingly depending on the induced flow 261
velocity. In general, the *dt* was set to maintain a maxi- 262
mum particle displacement of 5–7 pixels, with the value 263
ranging from 48 to 22 μs (voltage/velocity dependant). 264
LaVision's ImagerProX 4 M (2,048 × 2,048 pixels) 265
camera fitted with a 105-mm lens was used to capture the 266
PIV images. The field of view for each image was 267
approximately 48 mm × 48 mm (*x*, *y*). 268
LaVision's DaVis 7.2 PIV software package was used to 269
calibrate, capture, pre-process, process, and post-process 270
the PIV images. Image calibration was performed with a 271
40 mm × 40 mm, two-tiered calibration plate. In pro- 272
cessing the PIV data, the local average intensity was 273

Fig. 5 Convergence plot for the *x*-component of velocity ($\bar{U}_x$) for two locations in the flow field (14 kHz driving frequency). **a** Point $(x, y) = (5, 0.5)$ mm and **b** $(x, y) = (35, 1.5)$ mm
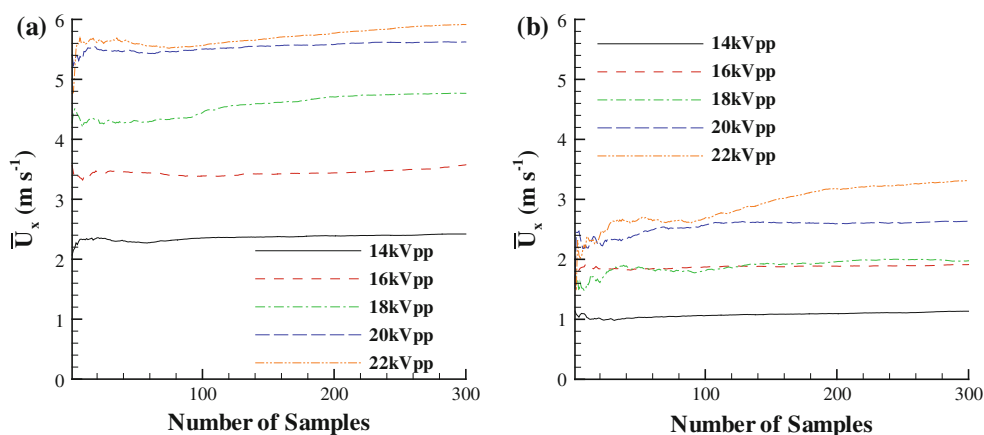
subtracted from the raw images in order to increase the relative contrast between the particles and the background. Furthermore, a local particle intensity correction was applied in which the particle intensities are normalized over a window of 4 pixels, allowing smaller particles to contribute more effectively in the correlation. Having masked the surface of the actuator, each image pair was then subjected to a cross-correlation multi-grid procedure. The correlation process consisted of an initial pass with a 32×32 pixel^2 interrogation window with a 50 % overlap, followed by two refining passes with 16×16 pixel^2 widows again with 50 % overlaps. For the initial pass, a 1:1 Gaussian weight was applied to the integration widows, while a 2:1 was applied on the refining passes. This resulted in a resolution of 5.26 vectors per mm. Outliers were detected and removed using a recursive spatial outlier detection (Westerweel 1994) in between multi-grid passes as well as on the final vector field.

For each input voltage, 300 image pairs were taken at a repetition rate of 7.2 Hz. Typical convergence plots of the mean tangential velocity component ($\bar{U}_x$) are shown in Fig. 5a and b for two locations in the velocity field. The first point, (5, 0.5) mm, is representative of the high velocity region near the discharge (Fig. 5a), while the second position, (35, 1.5), is within the fully developed wall jet (Fig. 5b). After ~ 200 samples, the average values begin to converge to a constant value for both points. The relative statistical uncertainty ζ for these two points is shown in Fig. 6 as calculated from

$$\zeta = \frac{t_{N-1,95\,\%}\,\bar{\sigma}_x}{\bar{U}_x} \tag{2}$$

where $t_{N-1,95\,\%}$ is the *t estimator* ($N - 1$ degrees of freedom, 95 % confidence interval), $\bar{\sigma}_x$ is the standard deviation of the mean velocity, and $\bar{U}_x$ is the mean velocity (*x*-component). The results indicate a maximum relative error of ~ 4 % in the velocity measurements.
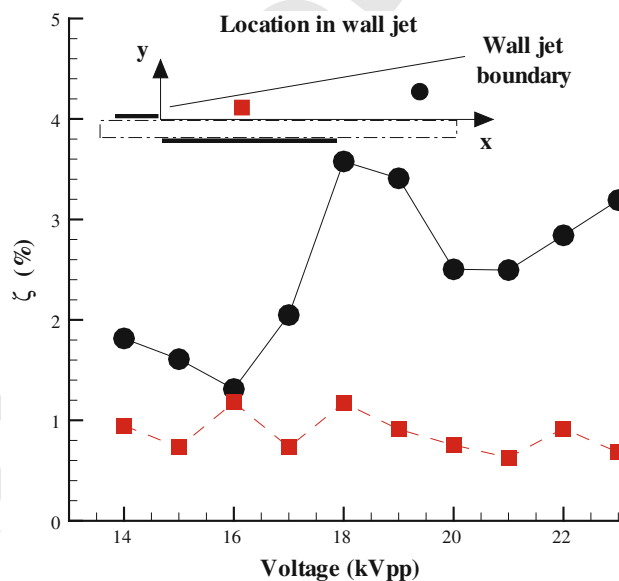

Fig. 6 Relative statistical uncertainty as a function of voltage and position for the velocity vector field (14 kHz driving frequency). *Red squares* correspond to point $(x, y) = (5, 0.5)$ mm while *black circles* represent $(x, y) = (35, 1.5)$ mm

3.1.1 PIV seeding

For the experiments outlined in this text, Ondina oil was used as the seeding particles. The oil was vaporized using a TSI atomizer (Model 9302) which, when pressurized at 25 psi, produces a droplet with a mean diameter of $\sim 0.8\ \mu$m (TSI 2000). Assuming a characteristic velocity of 5 m s^{-1}, a reference length of 1 mm, and Stokesian drag, the Stokes number (*St*) as defined by Adrian and Westerweel (2011) is 7.8×10^{-3} (or $St \ll 1$), indicating a reasonable fluidic response from the particles.

For plasma actuation, however, consideration of the electrodynamic influence on the particles is also warranted due to the presence of the large electric fields required to initiate the discharge. In doing so, the PIV images may be

broken into two regions: (1) the discharge volume itself and (2) the far-field away from the vicinity of the discharge. Within the discharge volume, a charging of the particle could result in a combination of fluidic and Coulombic forces influencing the particle's path. In the far-field, however, the dominant electrodynamic effect would likely be a dielectrophoretic force due to polarization of the particle. This is a topic which certainly remains an open area for future exploration as an electrodynamic influence on the seeding particles could potentially alter the accuracy of the velocity measurement and consequently the inferred thrust. Here, however, we will rely on a comparison of the vector field with and without seeding particles.

To investigate any potential electrodynamic effects on the seeding particles, the PIV velocity profiles were compared against measurements obtained using a Pitot (pressure) probe. The probe used was a United Sensor Corp. stainless steel "boundary layer probe" (Model BR-.025-12-C-11-.120) having an inner and outer diameter of 0.4318 and 0.635 mm, respectively. The design of the probe's tip, however, is flattened (the diameter is reduced by half), which significantly reduces its presence in the wall normal direction. Positioning of the probe was controlled using a two-axis traverse (Velmex MN10-0150-M02-21) with a minimum step size of 5 μm. The pressure measurements were made using a Furness Controls FCO332 differential manometer calibrated to ±25 Pa with a ±10 V output. Each data point represents the average of 800 voltage readings recorded at a sampling rate of 20 Hz using a National Instruments data acquisition module (PCI-6133). The differential pressure, ΔP, measurements were converted to velocities using Eq. 3 where ρ is the air density. Here, the air density was taken as 1.184 kg m^{-3} which corresponds to a laboratory temperature of 25 °C. An error analysis was carried out on the obtained data which took into account the accuracy of

the transducer (±0.5 % Pa), the accuracy of the voltage reading (±5 mV), and the statistical uncertainty of the sampled set.

$$U_x = \sqrt{2\Delta P \big/ \rho} \tag{3}$$

The use of a metallic probe limited the proximity in which a measurement may be made near the plasma. Furthermore, measurements near the dielectric surface were also prohibited as arcing was observed between the probe and the dielectric when the probe itself was in contract with surface. These problems were alleviated, however, by taking readings sufficiently far downstream (25 and 35 mm) and keeping the probe away the dielectric surface (>0.5 mm). As shown in Fig. 7, reasonably good agreement is seen between the two data sets both in terms of magnitude and shape giving some indication that electrodynamic effects may be negligible in the current experimental setup

3.1.2 Inferred thrust calculation

The rectangular control volume as depicted in Fig. 8 was applied to the time-averaged velocity field generated from the PIV measurements. The net thrust, T_x and T_y, produced by the actuator (normalized by the electrode length) is determined from the conservative form of the momentum equations assuming time independence (Eq. 4a, b). The net thrust produced would be the summation of the wall shear stress (F_s), pressure differential, and the plasma-induced body force (F_p), acting within and on the control volume. If the control volume boundaries are significantly removed from the bulk plasma, a constant pressure assumption may be made (Kotsonis et al. 2011), in which the net thrust in the x-direction would be equal to $T_x = F_{x,p} - F_s$. In this

Fig. 7 Comparison between pitot measurements and PIV profiles taken at (**a**) 25 and (**b**) 35 mm downstream of the exposed electrode for an applied voltage of 20 kVpp at 14 kHz
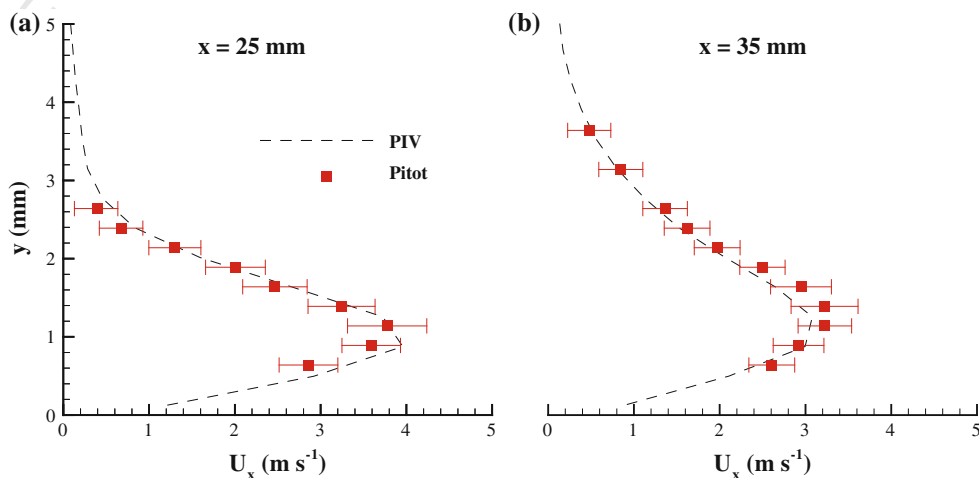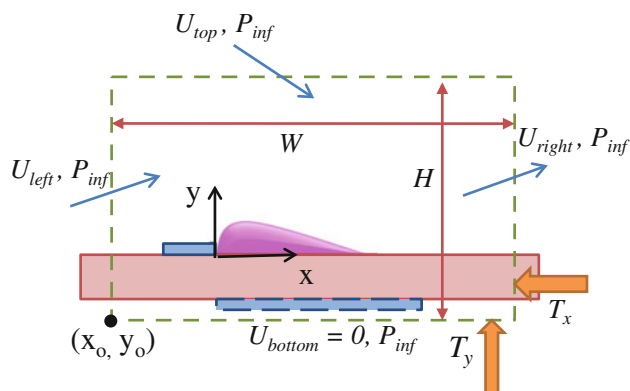
Fig. 8 Schematic of control volume used to calculate reaction forces induced by the plasma discharge

391 analysis, however, we are interested in only the net thrust
392 imparted to the dielectric. The control volume used is
393 drawn accordingly to negate such distinctions. In partic-
394 ular, the boundaries of the volume extend below the
395 dielectric surface where the velocity field is zero, to
396 emphasis that the wall shear stress is not considered as a
397 separate force. The thrust components are calculated from
398 the velocity field as follows:

$$T_x = -\int_{y_o}^{H} \rho U_{x,\text{left}}^2 dy + \int_{x_o}^{W} \rho U_{x,\text{top}} U_{y,\text{top}} dx + \int_{y_o}^{H} U_{x,\text{right}}^2 dy \tag{4a}$$

400

$$T_y = -\int_{y_0}^{H} \rho U_{y,\text{left}} U_{x,\text{left}} dy + \int_{x_0}^{W} \rho U_{y,\text{top}}^2 dx$$
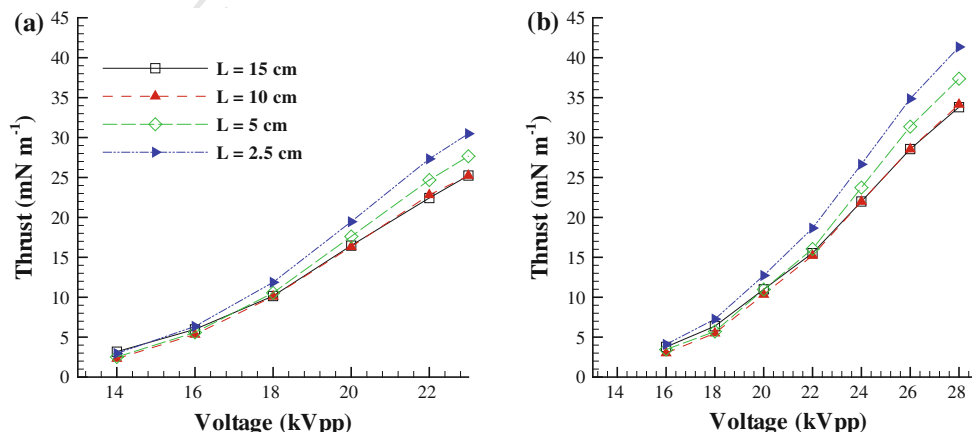$$+ \int_{y_0}^{H} \rho U_{y,\text{right}} U_{x,\text{right}} dy \tag{4b}$$

402

4 Results

4.1 Influence of the actuator plate length

In order to evaluate the effect of the actuator's plate
length (L), shown in Fig. 1b, different plate lengths were
tested. The same actuator was used throughout the
experiments with the plate length, L, being reduced each
time. Lengths corresponding to 15, 10, 5, and 2.5 cm
were investigated over a range of voltages (14–28 kVpp).
A plate length of 15 cm was chosen as to mimic the plate
length of the actuator used in the control volume analysis.
A limiting length of 2.5 cm was imposed to avoid the
possibility of arcing around the dielectric substrate, since
the encapsulated electrode itself is 2-cm wide. The
lengths 10 and 5 cm were chosen arbitrarily as incre-
mental lengths.

The results of this study, presented in Fig. 9, indicate
that there is little variation in the resultant thrust regard-
less of the length of the plate for lower input voltages.
This trend does not hold, however, as the voltage
increases. At the higher voltages investigated, an increase
in thrust, as the actuator's plate length is
decreased, is observed. This increase is independent of the two fre-
quencies investigated. At the maximum voltages tested, a
difference of 5 and 7 mN/m was measured between plate
lengths of 15 cm and 2.5 cm for 14 kHz and 7 kHz,
respectively. This corresponds to a ∼20 % increase in
measured thrust in both cases (Fig. 10). Such a large
discrepancy could prove problematic when trying to
compare between different researchers' results if the plate
length was not specified.

Because the viscous drag rapidly decreases in the
downstream direction as the induced wall jet expands and
dissipates, the difference in its integrated effect becomes
less severe as the plate length is increased beyond a certain

Fig. 9 Force measurements over a range of input voltages with varying actuator plate lengths: **a** 14 kHz and **b** 7 kHz
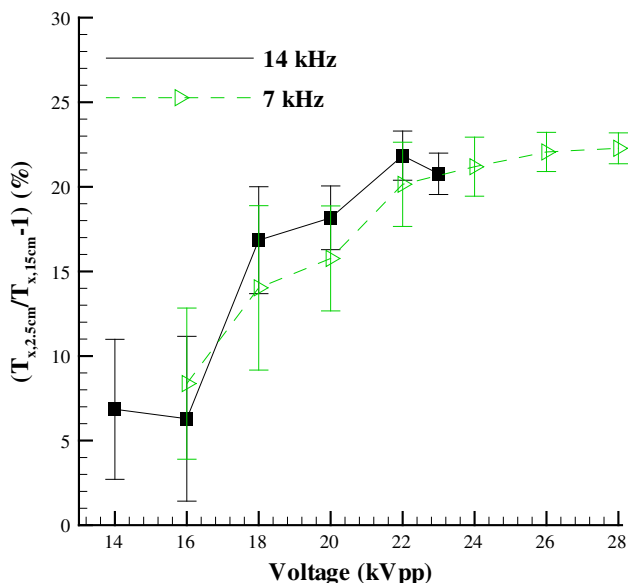
Fig. 10 Percentage increase in thrust between a plate length of 2.5 and 15 cm as a function of voltage
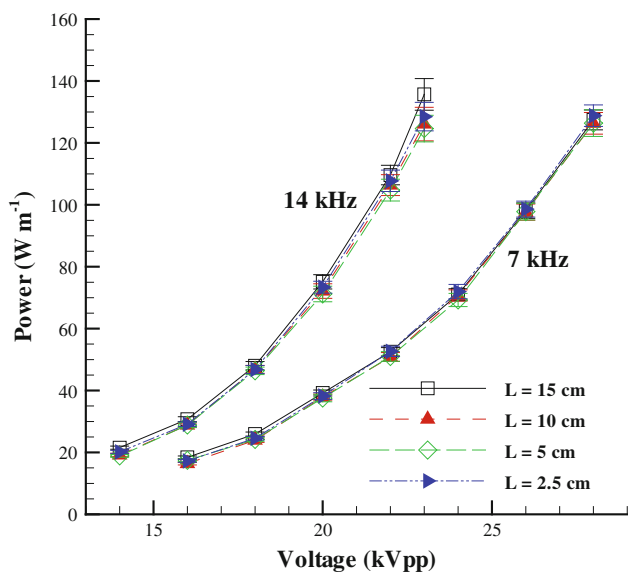
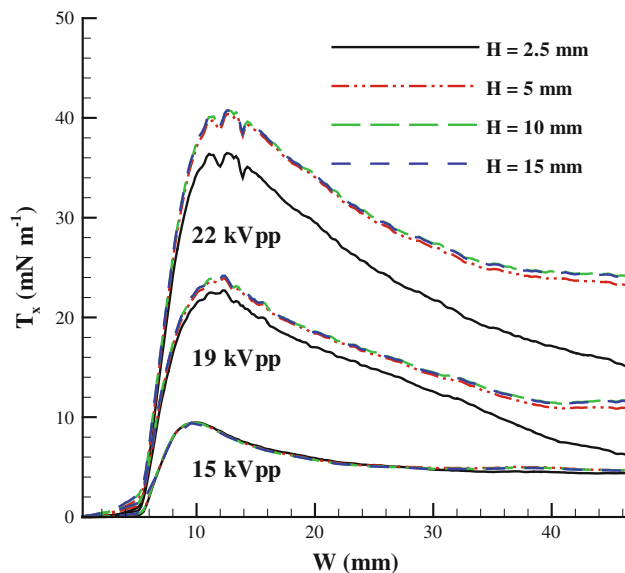**Fig. 11** Power dissipation as a function of voltage for different plate lengths

Fig. 12 Resultant tangential thrust component for a 15, 19, and 22 kVpp input voltage at 14 kHz as function of the width ($W = x - x_o$) for varying heights ($H = y - y_o$) of the control volume

threshold (e.g. $L = 10$ cm). This results in nearly identical (plate-independent) thrust values for the longer plate lengths ($L = 10$ cm and 15 cm). For shorter plate lengths, however, the impact of the viscous drag overall would be significantly less than the longer plates, resulting in higher recoverable thrust readings. It is also plausible that a shortening of the dielectric plate affects the surface charge accumulation and thus the electric field and induced force on the fluid. A substantial surface charge has been shown to persist several centimeters downstream of an actuator (Opaits et al. 2008; Enloe et al. 2008a, b). Regardless of the

exact mechanism, Fig. 11 verifies that the power consumption and thus power delivered to the plasma load remains constant regardless of the plate length, indicating a nominal constant body force is generated.

4.2 Control volume extracted forces

In order to extract the reaction thrusts on the control volume, the integrals on the right-hand side of Eq. 4a and b were numerically integrated in Matlab using the time-averaged PIV data. A composite trapezoidal rule was used for the integration scheme. It was found that the starting x-location, x_o, in the integrals had little influence on the resultant thrust calculated as long as it was chosen behind the edge of the exposed electrode (i.e. $x_o < x = 0$, referring to Fig. 8). The starting y-location, y_o, was chosen arbitrarily below the dielectric material such that $y_o < 0$ (Fig. 8). The starting locations used were -5.0 and -0.1 mm corresponding to x_o and y_o, respectively. Also, it is pertinent to note that a constant air density (ρ) is assumed. This assumption was also made by Hoskinson et al. (2008) based on prior experimental data from Enloe et al. (2006). In this prior work, it was estimated that the density fluctuations near the actuator were less than 2 % of ambient. Again, the air density was taken as 1.184 kg m^{-3}.

Figure 12 depicts typical plots of the inferred tangential thrust component, T_x, and how it varies with the width ($W = x - x_o$) and the height ($H = y - y_o$) of the control volume (referring to Fig. 8) for various voltages. The plot indicates that the thrust is independent of the control volume's height beyond a given point (10 mm for all cases

investigated). This point corresponds to the total encapsulation of the induced wall jet's "boundary layer". The boundary layer created by the jet increases with both applied voltage and downstream location. However, for the range of voltages investigated, the boundary layer was less than 10-mm thick for the given field of view. More important than the height of the control volume is its width, as Fig. 12 reveals. The calculated net thrust is highly dependent on the point at which the control volume ends. If the width is too small, the thrust may be grossly over-predicted as compared to a much wider control volume.

The tangential and normal thrust components are plotted in Fig. 13a and b, respectively, over the range of input voltages investigated. At each voltage, the thrust was extracted for five different control volume widths from data similar to Fig. 14. The vertical dashed lines in Fig. 14 correspond to control volume widths of 10, 20, 30, 40, and 45 mm. The height of the control volume chosen was 10 mm, which is a suitable choice for reasons previously discussed. Over the range of supplied voltages, the calculated tangential thrust shows a strong dependency on the width of the control volume. This dependency becomes more pronounced at higher voltages. The calculated thrusts do begin to plateau as the downstream extent of the control volume is increased. This is a result of the asymptotic

nature of the curves shown in Fig. 12. We note that the thrust does continually decrease as the downstream extent is increased due the perpetual addition of viscous drag. However, the rate of this decrease begins to slow as the wall jet expands and dissipates.

The normal thrust component deviates from this trend with its values remaining approximately constant as the width of the control volume is increased (Fig. 13b). The exception, however, to this observation is the smallest control volume plotted ($W = 10$ mm). Regardless, the magnitude of the normal component is significantly less than that of the tangential. The large disparity between the normal and tangential components is in line with other reports (Cheong et al. 2011).

4.3 Comparison between the two measurement methods

A comparison between the control volume analysis and the direct thrust measurement is shown in Fig. 15. Two different control volume widths ($W = 20$ and 40 mm) are presented, as well as the plate-independent direct thrust measurements ($L = 10$ cm). Results indicate that the measured and inferred thrusts are in good agreement over the entire voltage range for the wider ($W = 40$ mm) control

Fig. 13 Forces calculated from a control volume analysis as a function of voltage for various widths ($W = x - x_o$) of the control volume (14 kHz): **a** tangential component of force (Tx) and **b** normal component of force (Ty)
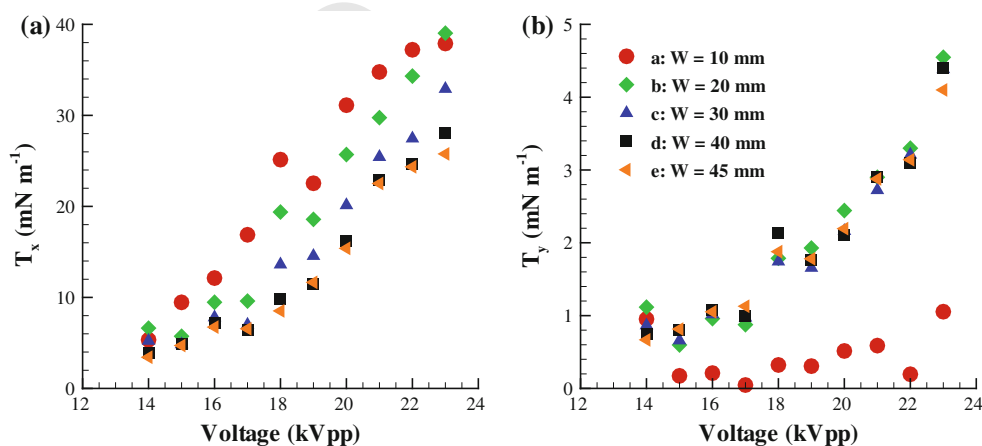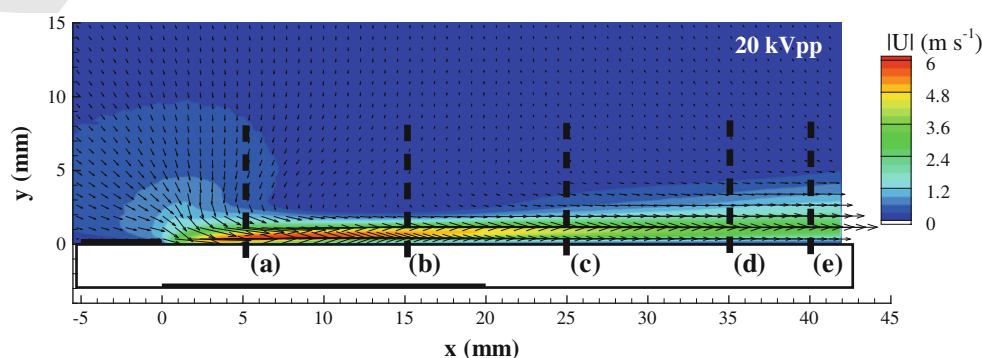
Fig. 14 Velocity magnitude contour for 20 kVpp input driven at 14 kHz. The *dashed lines* labeled (**a**) through (**e**) correspond to control volume widths ($W = x - x_o = x - (-5)$ mm) of 10, 20, 30, 40, and 45 mm, respectively
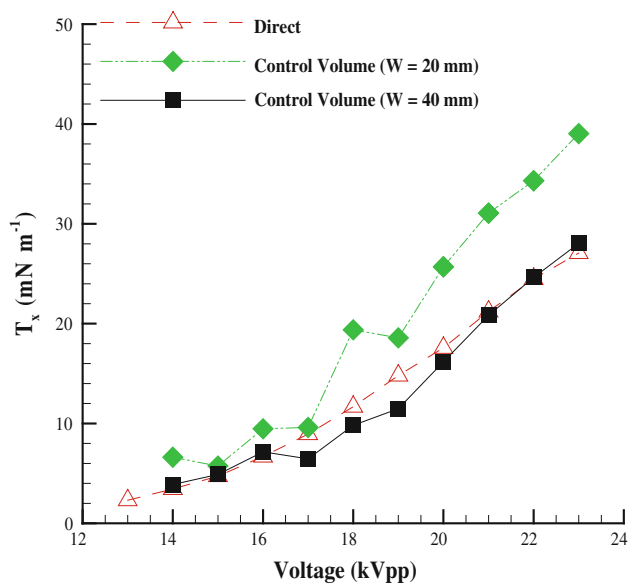
Fig. 15 Comparison between direct thrust measurements and those inferred from a control volume analysis. The driving frequency was 14 kHz

525 volume. It is also evident that if the control volume is of
526 insufficient size, the thrust may be over-predicted and
527 eludes that there is a minimum length downstream of the
528 actuator that the control volume needs to consider. That
529 length, however, is directly tied to the applied voltage as
530 there is a decent agreement for the smaller control volume
531 width at lower input voltages. Based on these results, a
532 downstream extension of ~ 35 mm is recommended.

533   Identifying the plate-independent direct thrust with a
534 single parameter could be useful for practical purposes. A
535 non-invasive parameter of choice, as suggested by Krieg-
536 seis et al. 2011b, is the plasma length (L_p) which results
537 from the combination of geometric and electrical inputs.
538 The plasma length was determined from photographs
539 obtained using a Nikon D90 digital camera fitted with a
540 105-mm lens (8-s exposure, f/7.1). The color images were
541 first converted to grayscale, then binarized using a

542 threshold value of 0.08. A tracing algorithm then mapped
543 out the plasma, and an average value was determined. This
544 value is plotted in Fig. 16a against the plate-independent
545 direct thrust measurements for $L = 10$ cm presented in
546 Fig. 15. A linear relationship was found between the direct
547 thrust data ($T_{x,\text{Direct}}$) in mN m^{-1} and the plasma length (L_p)
548 in mm.

$$T_{x,Direct} = 6.57L_p - 18.9 \tag{5a}$$

550   To determine the minimum threshold for the control
551 volume size for reasonably predicting thrust, the same
552 scaling metric (L_p) was studied. A linear relation of the
553 form

$$x_{min} = 7.12L_p - 11.1 \tag{5b}$$

555 was obtained for the minimum control volume's down-
556 stream extent ($x_{\min} = W_{\min} + x_o$). This relation was found
557 by matching the direct thrust data from Fig. 15
558 ($L = 10$ cm) with PIV inferred thrust data, represented in
559 Fig. 12, for given voltages. The difference between the
560 inferred thrust using the minimum control volume exten-
561 sion and the direct measurements are provided in Fig. 16b
562 on a percentage basis. As a comparison, the percentage
563 difference in using a fixed control volume is also shown. In
564 general (with exception of the lower voltages), using the
565 minimum control volume extent yields better or similar
566 results to that of the fixed width volume for $W = 40$ mm.
567 Furthermore, the plot also emphasizes the over-prediction
568 of the thrust when using a control volume of insufficient
569 size (in this case $W = 20$ mm).

4.4 Energy conversion efficiency

571 The device characterization of an actuator tested in qui-
572 escent conditions is not complete without an understanding
573 of its energy conversion efficiency, η, which is defined as
574 (Zito et al. 2012) the ratio of thrust (T_x) and induced
575 maximum velocity ($U_{x,\text{ max}}$) to that of the delivered power
576 (P):

Fig. 16 a Thrust as a function plasma length and **b** the percent difference between direct and control volume inferred forces using a fixed and scaled control volume
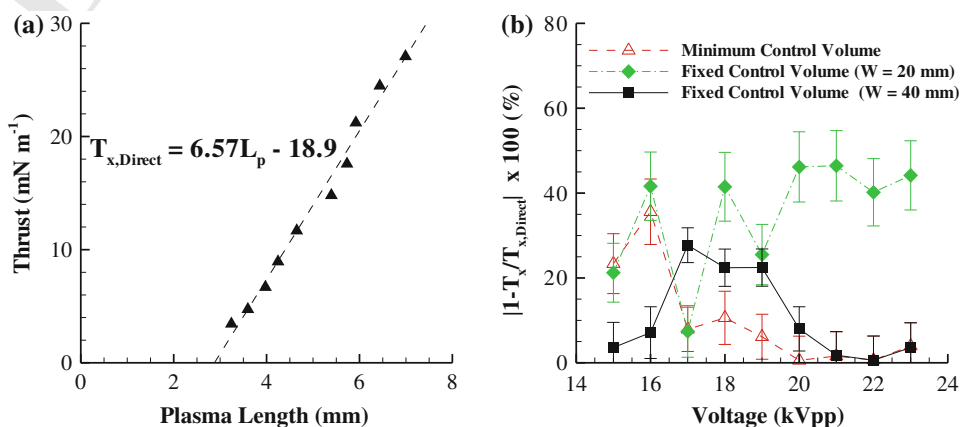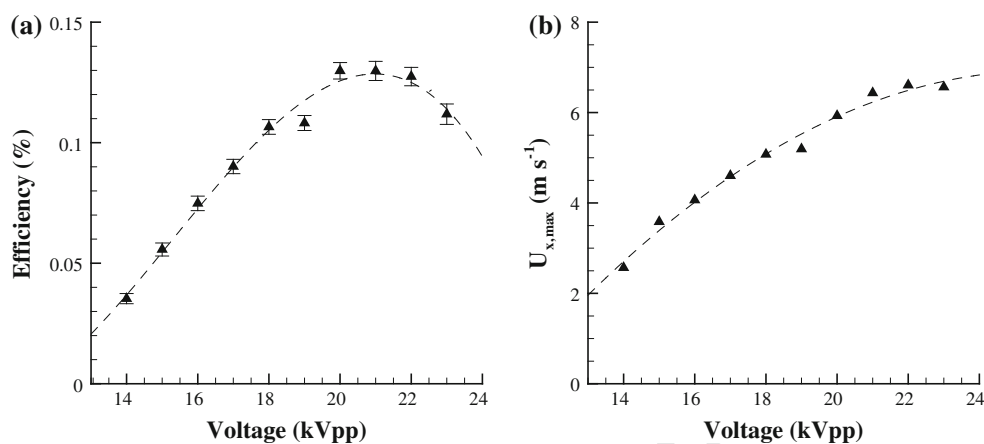
Fig. 17 **a** Energy conversion efficiency and **b** peak-induced velocity of a DBD actuator made from a 3-mm-thick acrylic plate operating at 14 kHz

$$\eta = \frac{T_x U_{x,\max}}{P} \qquad (6)$$

578 The calculated efficiency for the actuator geometry used
579 in this text for a driving frequency of 14 kHz is plotted as a
580 function of the applied voltage in Fig. 17a, with the
581 maximum velocity extracted from collected PIV data
582 shown in Fig. 17b. While the efficiency of the DBD
583 actuator is less than 0.15 %, the results show a peak
584 efficiency region for the device. As the voltage is further
585 increased, the induced velocity saturates and the efficiency
586 drops implying more power loss in dielectric heating and/
587 or streamer formation.

588 **5 Conclusion**

589 The effect of varying the plate length upon which the
590 plasma-induced wall jet acted was investigated using a
591 direct force balance. At the upper range of the voltages
592 investigated, an increase in thrust was observed as the plate
593 length was decreased. The thrust was nearly identical for
594 10- and 15-cm length, but an increase in thrust of 20 % was
595 observed as the plate length was reduced to 2.5 cm (a four
596 to six times reduction). Based on these findings, the plate's
597 length is an important consideration for making compari-
598 sons between various reported experimental data. PIV
599 measurements were also made on a single actuator plate for
600 various voltages. These measurements provided time-
601 averaged data sets of the induced flow field. The velocity
602 fields were then subjected to a control volume analysis to
603 infer the resultant thrusts acting on the rectangular volume.
604 The results of the analysis indicated a strong dependency
605 on the size of the considered volume with a particular
606 emphasis on the width of it. When compared with the
607 direct thrust measurements, the calculated tangential thrust
608 agreed well regardless of input voltage if the control vol-
609 ume extended far enough downstream. Also, the discharge
610 length was optically measured using visible light emission.

611 A linear correlation was found between the plasma length
612 and the measured thrust for the actuator configurations
613 studied. A suitable control volume size was also recom-
614 mended based on the plasma length. Finally, to complete
615 the device characterization, the energy conversion effi-
616 ciency curve for a representative actuator is also plotted.

621 **References**

622 Abe T, Takizawa Y, Sato S, Kimura N (2008) Experimental study for
623 momentum transfer in a dielectric barrier discharge plasma
624 actuator. AIAA J 46(9):2248–2256
625 Adrian RJ, Westerweel J (2011) Particle image velocimetry. Cam-
626 bridge University Press, Cambridge
627 Baughn JW, Porter CO, Peterson BL, McLaughlin TE, Enloe CL,
628 Font GI, Baird C (2006) Momentum transfer for an aerodynamic
629 plasma actuator with an imposed boundary layer. In: 44th AIAA
630 aerospace sciences meeting. AIAA 2006-168
631 Borghi CA, Carraro MR, Cristofolini A, Neretti G (2008) Electro-
632 hydrodynamic interaction induced by a dielectric barrier dis-
633 charge. J Appl Phys 103(6):063304
634 Cheong M, Greig A, Gibson B, Arjomandi M (2011) An investigation
635 into the effect of electric field on the performance of dielectric
636 barrier discharge plasma actuators. Exp Therm Fluid Sci
637 35(8):1600–1607
638 Corke TC, Post ML, Orlov DM (2007) Sdbd plasma enhanced
639 aerodynamics: concepts, optimization and applications. Prog
640 Aerosp Sci 43(7–8):193–217
641 Debien A, Benard N, David L, Moreau E (2012) Unsteady aspect of
642 the electrohydrodynamic force produced by surface dielectric
643 barrier discharge actuators. Appl Phys Lett 100(1):013901. doi:
644 10.1063/1.3674308
645 Enloe CL, McLaughlin TE, Vandyken RD, Kachner KD, Jumper EJ,
646 Corke TC (2004) Mechanisms and responses of a single
647 dielectric barrier plasma actuator: plasma morphology. AIAA J
648 42(3):589–594
649 Enloe CL, McLaughlin TE, Font GI, Baughn JW (2006) Parameter-
650 ization of temporal structure in the single-dielectric-barrier
651 aerodynamic plasma actuator. AIAA J 44(6):1127–1136

Enloe CL, Font GI, McLaughlin TE, Orlov DM (2008a) Surface potential and longitudinal electric field measurements in the aerodynamic plasma actuator. AIAA J 46(11):2730–2740

Enloe CL, McHarg MG, McLaughlin TE (2008b) Time-correlated force production measurements of the dielectric barrier discharge plasma aerodynamic actuator. J Appl Phys 103(7):073302

Enloe CL, McHarg MG, Font GI, McLaughlin TE (2009) Plasma-induced force and self-induced drag in the dielectric barrier discharge aerodynamic plasma actuator. In: 47th AIAA aerospace sciences meeting including the new horizons forum and aerospace exposition. AIAA 2009-1622

Font GI, Enloe CL, McLaughlin TE (2010) Plasma volumetric effects on the force production of a plasma actuator. AIAA J 48(9):1869–1874. doi:10.2514/1.51660

Font GI, Enloe CL, Newcomb JY, Teague AL, Vasso AR, McLaughlin TE (2011) Effects of oxygen content on dielectric barrier discharge plasma actuator behavior. AIAA J 49(7):1366–1373. doi:10.2514/1.55031

Forte M, Jolibois J, Pons J, Moreau E, Touchard G, Cazalens M (2007) Optimization of a dielectric barrier discharge actuator by stationary and non-stationary measurements of the induced flow velocity: application to airflow control. Exp Fluids 43:917–928. doi:10.1007/s00348-007-0362-7

Gibalov VI, Pietsch GJ (2000) The development of dielectric barrier discharges in gas gaps and on surfaces. J Phys D Appl Phys 33(20):2618

Gibson BA, Arjomandi M, Kelso RM (2012) The response of a flat plate boundary layer to an orthogonally arranged dielectric barrier discharge actuator. J Phys D Appl Phys 45(2):025202

Grundmann Sven, Tropea Cameron (2009) Experimental damping of boundary-layer oscillations using dbd plasma actuators. Int J Heat Fluid Flow 30(3):394–402

Hoskinson AR, Hershkowitz N (2010) Differences between dielectric barrier discharge plasma actuators with cylindrical and rectangular exposed electrodes. J Phys D Appl Phys 43(6):065205

Hoskinson AR, Hershkowitz N, Ashpis DE (2008) Force measurements of single and double barrier dbd plasma actuators in quiescent air. J Phys D Appl Phys 41(24):245209

Jolibois J, Moreau E (2009) Enhancement of the electromechanical performances of a single dielectric barrier discharge actuator. Dielectr Electr Insulation IEEE Trans 16(3):758–767

Jukes TN, Choi K-S (2009) Long lasting modifications to vortex shedding using a short plasma excitation. Phys Rev Lett 102:254501

Kogelschatz U (2003) Dielectric-barrier discharges: their history, discharge physics, and industrial applications. Plasma Chem Plasma Process 23:1–46. doi:10.1023/A:1022470901385

Kotsonis M, Ghaemi S, Veldhuis L, Scarano F (2011) Measurement of the body force field of plasma actuators. J Phys D Appl Phys 44(4):045204

Kriegseis J (2011a) Performance characterization and quantification of dielectric barrier discharge plasma actuators. Ph.D thesis, TU Darmstadt

Kriegseis J, Grundmann S, Tropea C (2011b) Power consumption, discharge capacitance and light emission as measures for thrust production of dielectric barrier discharge plasma actuators. J Appl Phys 110(1):013305

Labergue A, Moreau E, Zouzou N, Touchard G (2007) Separation control using plasma actuators: application to a free turbulent jet. J Phys D Appl Phys 40(3):674

Little Jesse, Nishihara Munetake, Adamovich Igor, Samimy Mo (2010) High-lift airfoil trailing edge separation control using a single dielectric barrier discharge plasma actuator. Exp Fluids 48:521–537. doi:10.1007/s00348-009-0755-x

Opaits DF, Shneider MN, Miles RB, Likhanskii AV, Macheret SO (2008) Surface charge in dielectric barrier discharge plasma actuators. Phys Plasmas 15(7):073505

Post ML, Corke TC (2004) Separation control on high angle of attack airfoil using plasma actuators. AIAA J 42(11):2177–2184

Ramakumar K, Jacob JD (2005) Flow control and lift enhancement using plasma actuators. In: 35th AIAA fluid dynamics conference and exhibit. AIAA 2005-4635

Rizzetta DonaldP, Visbal MiguelR (2008) Plasma-based flow-control strategies for transitional highly loaded low-pressure turbines. J Fluids Eng 130(4):041104

Roth JR, Dai X (2006) Optimization of the aerodynamic plasma actuator as an electrohydrodynamic (ehd) electrical device. In: 44th AIAA aerospace sciences meeting and exhibit. AIAA 2006-1203

Roth JR, Sherman DM, Wilkinson SP (2000) Electrohydrodynamic flow control with a glow-discharge surface plasma. AIAA J 38(7):1166–1172

Schatzman DM, Thomas FO (2010) Turbulent boundary-layer separation control with single dielectric barrier discharge plasma actuators. AIAA J 48(8):1620–1634

Thomas FO, Kozlov A, Corke TC (2005) Plasma actuators for landing gear noise reduction. In: 11th AIAA/CEAS aeroacoustics conference (26th AIAA Aeroacoustics Conference). AIAA 2005-3010

Thomas FO, Kozlov A, Corke TC (2008) Plasma actuators for cylinder flow control and noise reduction. AIAA J 46(8):1921–1931

Thomas F, Corke T, Iqbal M, Kozlov A, Schatzman D (2009) Optimization of dielectric barrier discharge plasma actuators for active aerodynamic flow control. AIAA J 47(9):2169–2178

TSI (2000) Model 9302 atomizer, instruction manual. TSI Inc., St. Paul, MN

Westerweel J (1994) Efficient detection of spurious vectors in particle image velocimetry data. Exp Fluids 16:236–247. doi:10.1007/BF00206543

Xu X (2001) Dielectric barrier discharge—properties and applications. Thin Solid Films 390(1–2):237–242

Zito J, Durscher R, Soni J, Roy S, Arnold D (2012) Flow and force inducement using micro size dielectric barrier discharge actuators. Appl Phys Lett 100:193502